Photosynthesis Research (2024) 162:353–369
https://doi.org/10.1007/s11120-023-01057-3

RESEARCH

Tracking the first electron transfer step at the donor side of oxygen-evolving photosystem II by time-resolved infrared spectroscopy

Mohamad Yahia Dekmak[1] · Sarah M. Mäusle[1] · Janosch Brandhorst[1] · Philipp S. Simon[1,2] · Holger Dau[1]

Received: 17 August 2023 / Accepted: 24 October 2023 / Published online: 23 November 2023
© The Author(s) 2023

Abstract

In oxygen-evolving photosystem II (PSII), the multi-phasic electron transfer from a redox-active tyrosine residue (TyrZ) to a chlorophyll cation radical ($P680^+$) precedes the water-oxidation chemistry of the S-state cycle of the Mn_4Ca cluster. Here we investigate these early events, observable within about 10 ns to 10 ms after laser-flash excitation, by time-resolved single-frequency infrared (IR) spectroscopy in the spectral range of 1310–1890 cm^{-1} for oxygen-evolving PSII membrane particles from spinach. Comparing the IR difference spectra at 80 ns, 500 ns, and 10 µs allowed for the identification of quinone, P680 and TyrZ contributions. A broad electronic absorption band assignable $P680^+$ was used to trace largely specifically the $P680^+$ reduction kinetics. The experimental time resolution was taken into account in least-square fits of $P680^+$ transients with a sum of four exponentials, revealing two nanosecond phases (30–46 ns and 690–1110 ns) and two microsecond phases (4.5–8.3 µs and 42 µs), which mostly exhibit a clear S-state dependence, in agreement with results obtained by other methods. Our investigation paves the road for further insight in the early events associated with TyrZ oxidation and their role in the preparing the PSII donor side for the subsequent water oxidation chemistry.

Keywords Chlorophyll donor · Oxygen evolution · Photosynthesis · Redox-active tyrosine · System response function · Water oxidation

Introduction

Photosynthesis is a fundamentally important process to sustain aerobic life on planet Earth by (a) supplying organisms with chemical energy harvested from light energy and by (b) producing the oxygen we breathe. Artificial photosynthesis could contribute to mitigation of global climate change by sustainable production of non-fossil fuels, which is one of many reasons why studying the natural system in plants, cyanobacteria and algae is of interest to society (Dau et al. 2010; Cox et al. 2015). Photosystem II (PSII), one of the major protein complexes involved in oxygenic photosynthesis, is the catalyst that enables the splitting of two water molecules, whereby four electrons and four protons are removed from water (which are later used for generating chemical energy carriers) and O_2 is produced as a side-product (Dau and Zaharieva 2009; Vinyard and Brudvig 2017; Junge 2019; Lubitz et al. 2019; Cox et al. 2020; Shevela et al. 2023). PSII has been the subject of many research studies dating back as far as the 1970s, and the main principles of its reaction cycle have been well-established.

Following the absorption of a photon, charge separation is initiated at the primary electron donor chlorophylls (P680) involving electron transfer to a neighboring pheophytin molecule (Pheo), thereby generating the charge separated pair $P680^{\cdot+}/Pheo^{\cdot-}$ (for simplicity the symbol indicating the radical character of the groups will be omitted in the following). A series of electron transfer steps (depicted in Fig. 1A) leads to the oxidation of the Mn_4CaO_x cluster, which together with its surrounding amino acid residues and specific protein-internal water molecules comprises the oxygen evolving complex (OEC). Over a series of four absorption events,

✉ Sarah M. Mäusle
sarah.maeusle@fu-berlin.de

✉ Holger Dau
holger.dau@fu-berlin.de

1 Department of Physics, Freie Universität Berlin, Berlin, Germany

2 Molecular Biophysics and Integrated Bioimaging Division, Lawrence Berkeley National Laboratory, Berkeley, CA, USA

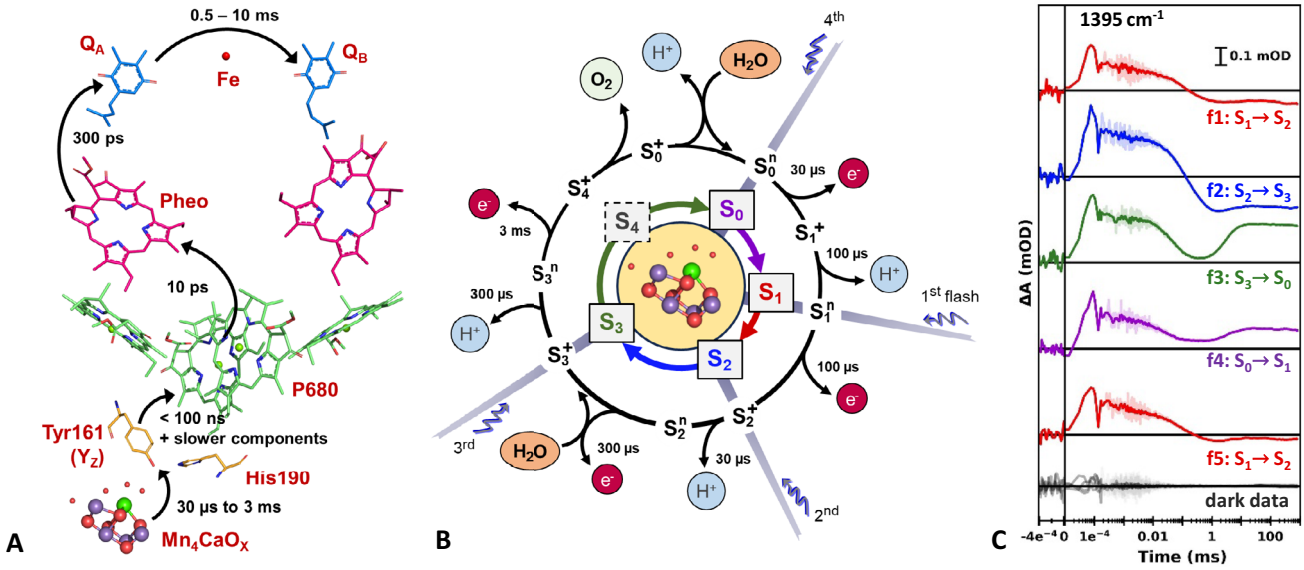

Fig. 1 Light-driven reaction cycle of Photosystem II. **A** Co-factors involved in the electron transfer pathway. The absorption of a photon leads to charge separation at the primary donor chlorophylls (P680). The electron moves via a pheophytin (Pheo) to plastoquinone Q_A and on to plastoquinone Q_B. A redox-active tyrosine residue (denoted as TyrZ or Y_Z) reduces $P680^+$ and is in turn reduced by the Mn_4CaO_x cluster, which accumulates oxidative equivalents over the course of four excitation events. **B** Extended S-state cycle scheme, depicting the oxidation state (subscript) and net charge state (superscript) of the Mn_4CaO_x cluster (S_0 denoting the most reduced state). Starting in the dark-stable S_1 state, four sequential excitation flashes lead to alternating removal of electrons (e^-) and protons (H^+), resulting in the release of molecular oxygen (O_2) after the third flash. During the $S_2 \rightarrow S_3$ and $S_3 \rightarrow S_0$ transitions substrate water molecules are inserted in the first coordination sphere of Mn ions. **C** Exemplary time-resolved IR transients of spinach PSII membrane particles at 1395 cm^{-1} for five sequential excitation flashes. Transients associated mainly with the $S_1 \rightarrow S_2$ transition is shown in red, $S_2 \rightarrow S_3$ in blue, $S_3 \rightarrow S_0$ in green, and $S_0 \rightarrow S_1$ in purple. The transparent lines show the original data; the darker lines show the same data after applying a smoothing algorithm (sliding average). Four transients, which were acquired in the absence of an excitation flash, are shown in black, illustrating the noise level. The data for $t > 0$ is shown on a logarithmic scale, while the IR signal over a period of 400 ns before the excitation flash are shown on a linear scale. The time constants indicated in (**A**) and (**B**) are approximate room-temperature values. The scheme in (**A**) and the Mn_4CaO_x cluster in the center of (**B**) were rendered in PyMOL using crystallographic data by Umena et al. (2011) (PDB ID: 3wu2). The hydrocarbon tails of some co-factors in (**A**) have been omitted for simplicity

the OEC accumulates the oxidative power required for the water splitting reaction by going through its so-called S-state cycle (Fig. 1B) (Kok et al. 1970). Beginning in the dark-stable S_1 state (S_0 to S_4, the subscript denoting the number of accumulated oxidizing equivalents), electrons and protons are removed alternatingly, thus keeping the overall charge (and redox potential) of the OEC stable (Dau and Haumann 2007; Klauss et al. 2012a). The final electron removal in the $S_3 \rightarrow S_4$ transition likely does not result in oxidation of a manganese as in all other transitions, but rather directly in the oxidation of an oxygen atom (Greife et al. 2023), but see also (Shevela et al. 2023).

The events at the OEC are preceded by several important electron transfer steps (Dau and Zaharieva 2009). On the electron acceptor side of PSII, charge separation is further stabilized by transferring the electron from $Pheo^-$ to a plastoquinone molecule, Q_A, within about 300 ps (Nuijs et al. 1986; Eckert et al. 1988). The electron remains at Q_A (Q_A stays reduced) for 0.5 to 10 ms, before being transferred to a second plastoquinone, Q_B, which unlike Q_A is not tightly bound to the protein. After having taken up two electrons (from two separate primary charge separation events), Q_B disassociates from PSII (carrying the electrons to other photosynthetic proteins) and is replaced by an oxidized Q_B molecule.

On the electron donor side of PSII, the redox-active tyrosine Y_Z has the important task of bridging the gap between P680 and the Mn_4CaO_x cluster. Around 50 years ago, Y_Z was still a mystery to be solved. Babcock and Sauer (1975) investigated an EPR signal named *Signal II_{fast}*, which was only later identified as originating from Y_Z, as reviewed by Styring et al. (2012). Despite the fact that the redox partner(s) had yet to be identified, it was then already observed that $P680^+$ reduction kinetics are multiphasic and S-state dependent (Gläser et al. 1976). Subsequent studies confirmed this, revealing $P680^+$ reduction kinetics spanning over four decades from tens of nanoseconds to hundreds of microseconds (Brettel et al. 1984; Schlodder et al. 1985). A slow S-state independent 200 µs phase was attributed to $P680^+/QA^-$ recombination (Schlodder et al. 1985; Christen et al. 1998), resulting in an unsuccessful S-state transition. A fast nanosecond phase of about 20–60 ns was found to be

more pronounced in the S_0 and S_1 states than in the S_2 and S_3 states, and some studies furthermore reported slightly slower time constants for the latter two states (Brettel et al. 1984; Meyer et al. 1989; Haumann et al. 1997; Ahlbrink et al. 1998; Jeans et al. 2002). It was found that this phase showed a relatively low activation energy of about 100 meV (Eckert and Renger 1988) and virtually no sensitivity to H_2O/D_2O exchange (Haumann et al. 1997; Ahlbrink et al. 1998; Schilstra et al. 1998). It was proposed (Eckert and Renger 1988) and later discussed in more detail (Christen and Renger 1999; Renger 2004) that this fast nanosecond phase could be linked to the fast movement of a proton between His190 and Y_Z, but is kinetically limited by an electron transfer (hence the lack of H/D kinetic isotope effect).

A slower nanosecond phase of about 100–800 ns was observed to be clearly more pronounced (Eckert and Renger 1988; Meyer et al. 1989; Lukins et al. 1996; Ahlbrink et al. 1998; Schilstra et al. 1998; Jeans et al. 2002) or even exclusively found (Brettel et al. 1984; Klauss et al. 2012b) in the S_2 and S_3 states. H_2O/D_2O exchange experiments again showed no kinetic isotope effect (Haumann et al. 1997; Ahlbrink et al. 1998; Schilstra et al. 1998), but the activation energy (~250 to 300 meV) was found to be higher than for the fast nanosecond phase (Jeans et al. 2002; Kühn et al. 2004; Klauss et al. 2012b). This slow nanosecond phase was interpreted as a local "dielectric" relaxation process (Renger 2004) and later also as nuclear rearrangements resulting in a contraction of about 50 $Å^3$ (Klauss et al. 2012b).

Besides the S-state independent 200 µs phase, two further microsecond phases of about 1–8 and 20–40 µs were reported, which were sensitive to H_2O/D_2O exchange and mostly exhibited strongest contributions in the S_2 and S_3 states (Schlodder et al. 1985; Eckert and Renger 1988; Lukins et al. 1996; Christen et al. 1998, 1999; Schilstra et al. 1998; Christen and Renger 1999). The microsecond kinetics have been interpreted as "large scale proton relaxation" events (Renger 2004). In Mn-depleted PSII samples the nanosecond kinetics are mostly absent and the $P680^+$ reduction kinetics are dominated by multiphasic microsecond phases (Haumann et al. 1997; Hays et al. 1999).

To gain insight into their structural environment, P680 and Y_Z have also been investigated with FTIR spectroscopy in inactive PSII samples (Zhang et al. 1997; Berthomieu et al. 1998; Noguchi et al. 1998). $P680^+$/P680 difference spectra confirmed that the radical cation charge of $P680^+$ is mainly localized on one chlorophyll (Okubo et al. 2007; Nagao et al. 2017), which is of significance as the charge localization impacts the redox potential (Takahashi et al. 2008). The $P680^+$/P680 difference spectra show a very broad spectral feature ranging from about 1000–6000 cm^{-1} assigned as an intervalence band (Okubo et al. 2007; Noguchi 2010) analogously a similar feature in bacterial reaction centers (Breton et al. 1992) and photosystem I (Breton et al. 1999), this broad band was attributed to an electronic transition originating from the dimeric nature of $P680^+$.

More recently FTIR has also been widely applied to intact PSII samples to observe the events of the S-state cycle, as reviewed in (Debus 2015; Noguchi 2015). With the exception of one extremely time-costly step-scan experiment (Greife et al. 2023), these studies are either steady-state measurements or have a time resolution limited to several milliseconds. In an alternative approach, time-resolved IR spectroscopy at single wavenumbers has been employed to observe PSII kinetics at the cost of spectral coverage (Noguchi et al. 2012; Takemoto et al. 2019; Mäusle et al. 2020). The flash-induced transients show distinctly different behavior after each of a sequence of flashes (Fig. 1C), demonstrating that kinetics related to the individual S-state transitions can be readily observed. $P680^+$ reduction kinetics have also been previously observed at 4000 cm^{-1} with microsecond time resolution (Sakamoto et al. 2017). By acquiring transients at individual wavenumbers over a large spectral region, we recently showed for PSI that we can obtain a time-resolved spectral data set in a relatively short measurement time with good a signal to noise ratio (SNR) (Mäusle et al. 2023).

We here report the first IR measurements of $P680^+$ reduction kinetics with sub-microsecond time resolution in intact oxygen evolving PSII membrane particles from spinach. By measuring the time-resolved IR difference signal at wavenumbers associated only with the broad electronic band (> 1760 cm^{-1}), we can observe the events at P680 without contributions of other groups. Double-difference spectra on the early-microsecond time scale of a time-resolved spectral data set furthermore allow us to obtain approximate P680 Yz^{ox}/ $P680^+$ Yz spectra in the 1310–1760 cm^{-1} region.

Materials and methods

Sample preparation

PSII membrane particles were prepared from spinach leaves as described previously (Schiller and Dau 2000), based on a protocol developed by Berthold, Babcock, and Yocum (Berthold et al. 1981). The oxygen evolution activity (> 1100 µmol O_2 per mg chlorophyll and hour) was measured with a Clarke-type electrode at 28 °C using 10 µg of Chl in 1 M betaine, 25 mM MES, 15 mM NaCl, 5 mM $CaCl_2$ (pH 6.2) buffer, 1 mM $K_3[Fe(CN)_6]$ and 0.25 mM DCBQ (2,6 dichloro-1,4-benzoquinone), of which the latter two ingredients serve as artificial electron acceptors. The sample was stored in 1 M betaine, 25 mM MES, 15 mM NaCl, 5 mM M_gCl_2, 5 mM $CaCl_2$ (pH 6.2) at – 80 °C. In preparation for an IR measurement (corresponding to 3 mg Chl) the sample was thawed on ice for an hour before resuspension in

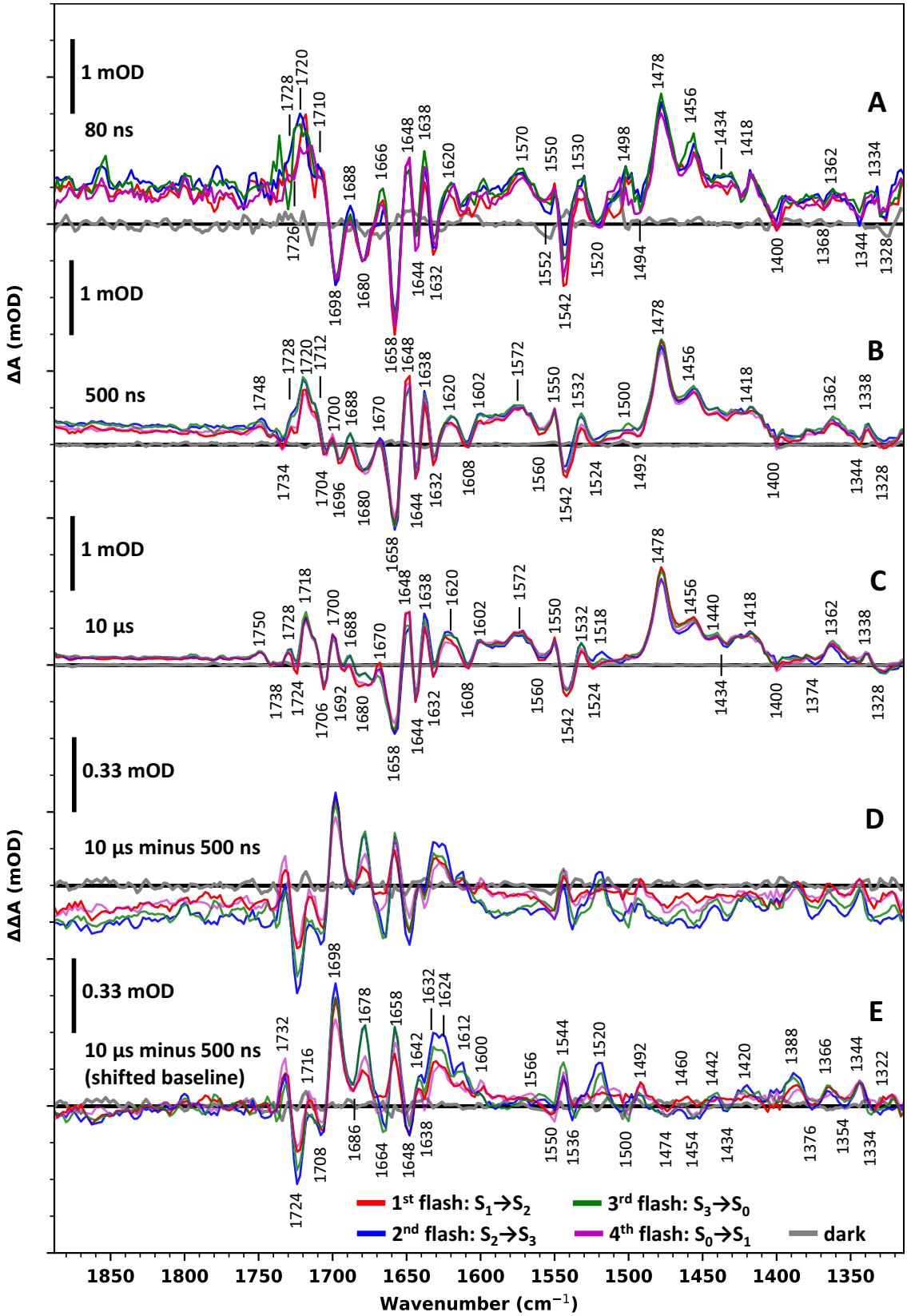
1 mOD
80 ns
A
1 mOD
500 ns
B
1 mOD
10 µs
C
0.33 mOD
10 µs minus 500 ns
D
0.33 mOD
10 µs minus 500 ns
(shifted baseline)
E
ΔA (mOD)
ΔΔA (mOD)
1st flash: S1→S2
2nd flash: S2→S3
3rd flash: S3→S0
4th flash: S0→S1
dark
1850 1800 1750 1700 1650 1600 1550 1500 1450 1400 1350
Wavenumber (cm−1)

◂**Fig. 2** Flash-induced time resolved IR difference spectra of spinach PSII membrane particles at 10 °C. The difference absorbance (ΔA) was obtained at every ~ 2 cm^{-1} between ~1310 and 1890 cm^{-1} by acquiring flash-induced transients; a sliding average over 3 neighboring wavenumber was applied, resulting in an effective spectral resolution of 6–8 cm^{-1}. Data associated mostly with the $S_1 \rightarrow S_2$ transition (first flash) is shown in red, the $S_2 \rightarrow S_3$ transition (second flash) in blue, the $S_3 \rightarrow S_0$ transition (third flash) in green and the $S_0 \rightarrow S_1$ (fourth flash) in magenta; the noise level is illustrated by 'dark spectra' (grey), obtained in the same way as the flash-induced data, but without applying an excitation flash. **A** IR difference spectra of around 80 ns after the first four excitation flashes. The spectra were obtained by averaging the data acquired between 50 and 110 ns. **B** IR difference spectra of around 500 ns (250–750 ns) after excitation. **C** IR difference spectra of around 10 µs (8–12 µs) after excitation. **D** Double difference spectra of the 10 µs spectra minus the 500 ns spectra (spectra C–spectra B). The resulting double difference absorption (ΔΔA) was small compared to the data shown in **A**, **B**, and **C** and was thus multiplied by a factor of 3 for better visualization (as indicated by the scale bar). **E** A baseline-corrected version of the double difference spectra shown in **D**, i.e. the spectra of 10 µs minus 500 ns. The non-smoothed spectral data (Fig. S3) as well as details of the two-step baseline correction can be found in Supplementary Information

the measurement buffer (identical to the storage buffer) and centrifuging for 12 min at 50.000×*g*. The supernatant was discarded and the same resuspension-centrifugation washing step repeated one more time. An artificial electron accepter PpBQ (phenyl-*p*-benzoquinone, 3 µl of 700 mM in dimethyl sulfoxide) was mixed with the resulting pellet. 10–12 mg of the pellet was squeezed between two CaF_2 plates with a 15 µm PTFE spacer; silicon grease was used on the edges of the plates for sealing. Per measurement day, 4–5 pairs of CaF_2 plates were mounted onto the automatic sample-exchange stage. All the above-mentioned steps were done under dim green light, otherwise the sample was kept in the dark.

IR measurements

The IR transients were measured using a quantum cascade laser (QCL) based time-resolved single-frequency (TRSFIR) setup described previously (Mäusle et al. 2020) which has since been modified as described elsewhere (Mäusle et al. 2023). The QCL (MIRcat-QT-Z-2300, Daylight Solutions, USA) is tuneable in the range between 1310 to 1890 cm^{-1}. A 5 ns frequency-doubled 532 nm Nd-YAG laser (Minilite II, Continuum, USA) was used for excitation and the signal from two 10 MHz pre-amplified mercury cadmium telluride (MCT) detectors (Vigo Systems, Poland) was recorded using 16-bit A/D converter (Spectrum, Germany) at a sampling rate of 65 MS/s. The sample compartment was cooled to 10 °C and flushed with dry air.

To synchronize the PSII membrane particles to the same S-state (S_1) before beginning the measurements, two saturating pre-flashes were applied to all sample spots, followed by an hour of dark-adaptation. For each of ~200 individual sample spots, the absorbance of the dark-adapted BBY sample was measured for a few seconds before a series of 10 saturating flashes at 1 Hz were applied. Following each 10-flash burst, the x–y-movable sample holder moved to a new dark-adapted sample spot. All transients are affected by a heat artefact, which was accounted for by acquiring the 10th flash IR transient with a threefold higher excitation energy and subsequently calculating and subtracting the heat signal as described previously (Mäusle et al. 2020), similar to an approach reported by Sakamoto et al. (2017). Time-resolved spectral information was obtained by performing the measurement sequentially at individual wavenumbers along the QCL range, in steps of 2 cm^{-1}. The final transients for individual wavenumbers were obtained by averaging of at least 20 transients. Originally 290 wavenumbers were measured between 1310 and 1890 cm^{-1}. Only 276 wavenumbers were used in the final spectra presented in this work, where the rest were omitted due to poor data quality. As the SNR of the individual transients was overall limited due to a low number of averages per transient, applying a sliding average smoothing algorithm (with a window size of three data points) along the wavenumber axis was necessary to obtain reasonably smooth spectra; this resulted in an effective spectral resolution of about 6–8 cm^{-1}.

Transients were fit in the range from 0 to 100 µs to a model defined by a sum of four exponentials parametrized as follows:

$$y(t) = y_o + a_1 e^{-t/\tau_1} + a_2 e^{-t/\tau_2} + a_3 e^{-t/\tau_3} + a_4 e^{-t/\tau_4}. \quad (1)$$

Additionally, an instrument response function (IRF) was taken into consideration which was iteratively convolved with the multi-exponential model during least-squares optimization (Python 3.9.2 and lmfit 1.2.2), as detailed in Sect. 1 of the SI. The IRF was approximated as

$$\mathrm{IRF}(\tau) = e^{\frac{-(\tau-\tau_o)^2}{2\sigma^2}}, \quad (2)$$

with σ = 17 ns (Mäusle et al. 2023) and t_0 = 44 ns. All data pre-processing was performed in Python 3.7.

Results

IR difference spectra related to $P680^+$/P680, Y_Z^{ox}/YZ and QA^-/QA

To investigate the kinetics preceding the events of the S-state cycle, we applied sequences of 10 saturating laser flashes to dark-adapted PSII membrane particles at ~276 individual wavenumbers ranging from 1310 to 1890 cm^{-1} (with a spacing of mostly 2 cm^{-1}). The flash-induced absorption changes

were recorded in the time range from nanoseconds to 800 ms; see Fig. 1C for exemplary high signal-to-noise data. From this data set, difference spectra can be constructed that correspond to distinct times after the respective laser flashes. In the present study, we focus on the spectra and reaction kinetics associated with fast $P680^+$ formation and its reduction by the redox-active tyrosine, Y_Z. In PSII with an intact oxygen-evolving complex, the latter is largely completed within 10 µs after the laser flash. Therefore, we focus on the events proceeding within 10 µs after the laser flash.

Difference spectra of around 80 ns (50–110 ns average) after the laser flash are shown in Fig. 2A, around 500 ns (250–750 ns) in Fig. 2B, and around 10 µs (8–12 µs) in Fig. 2C. All spectra are shown for the first four flashes applied to dark-adapted PSII, each of the four flashes initiating predominately one specific S-state transition, starting with $S_1 \rightarrow S_2$ (see also Fig. 1B). The spectra shown in Fig. 2 relate to the events following charge separation in PSII as follows:

(A) At 80 ns after the laser flash, the difference spectra reflect predominantly the formation of $P680^+$ and Q_A^- (Fig. 2A).
(B) In Fig. 2B, the difference spectra at about 500 ns are shown. At this time, the fast nanosecond phase of $P680^+$ reduction and Y_Z oxidation has resulted in strongly diminished $P680^+$/P680 contribution, whereas the amplitude of the Q_A^-/Q_A difference can be expected to be undiminished when compared to the 80 ns spectra of Fig. 1A.
(C) At 10 µs, the $P680^+$ reduction is mostly completed so that the corresponding difference spectra in Fig. 2C are composed of the Y_Z^{ox}/Y_Z and Q_A^-/Q_A difference spectra. The Q_A^-/Q_A contribution is expected to be undiminished when compared to the 80 ns spectrum.
(D) Figure 2D shows the double-difference absorbance (ΔΔA) of the 10 µs spectrum minus the 500 ns spectrum (C minus B). The ΔΔA spectrum corresponds exclusively to $P680^+$ reduction and Y_Z oxidation and thus represents the sum of Y_Z^{ox}/Y_Z and $P680/P680^+$ difference spectra, without contributions from the Q_A^-/Q_A difference spectrum. (Note that $P680^+$/P680 peaks visible in A and B are inverted in the double difference spectra of D and E).
(E) Figure 2E shows the same spectrum as shown in D but corrected for the time-dependent background shift, as detailed in Supplementary Information. For baseline correction, one constant was determined for each of the four spectra and then subtracted from all ΔΔA values of the respective spectrum. This procedure corresponds to subtraction of a baseline that is parallel to the x-axis. It represents an approximative approach here used to improve visibility of positive/negative peaks in the spectra and S-state dependent differences between spectra.

When comparing the S-state dependence (flash-number dependence) of the spectra in Fig. 2, we note minor difference in shape only but detect significant differences in the amplitude at early times. The amplitudes of positive and negative peaks are often larger in the second and third flash spectra than in the first and fourth flash spectra. A broad positive feature visible above 1750 cm^{-1} effectively results in a background shift of the spectra. This broad feature is most prominent in the early spectrum (Fig. 2A) and subsequently decays to smaller contributions, as can be easily observed by visually comparing Fig. 2A–C.

Comparing Fig. 2A–C, the positive peaks at 1362, 1418, around 1440, 1456, 1478 cm^{-1} and the negative peak at 1644 cm^{-1} show no clear change in their intensities over time, which is the expected behavior of quinones (see above). In addition, they show merely a weak or no presence in the double difference spectra (Fig. 2D and E). Consequently, we assign these peaks to the oxidized (Q_A, negative peak) or the singly reduced quinone (Q_A^-, positive peaks), in agreement with previous assignments (Hienerwadel et al. 1996; Zhang et al. 1997; Berthomieu et al. 1998; Suzuki et al. 2005). We detect further peaks likely related to the Q_A^- formation at 1328 (−), around 1572 (+), 1658 (−), and 1718 (+) cm^{-1}.

A negative peak at 1698 cm^{-1} (Fig. 2A) possibly downshifted to 1696 and 1692 cm^{-1} in Fig. 2B and C, respectively, displays a strong decrease in intensity over time. Although visually harder to detect because of the upshifted baseline, the negative peaks at 1552 and 1344 cm^{-1} exhibit a similar decaying behavior. All three features, however, show a clear positive band in the baseline-corrected double difference spectrum (Fig. 2E) and resemble peaks previously assigned to the 13^1-Keto C=O and chlorin ring vibrations of neutral P680 (Okubo et al. 2007). The positive signal around 1724 cm^{-1} (Fig. 2A) decays to around zero (Fig. 2C), resulting in a distinctly negative peak in Fig. 2E; a similar behavior is observed for the signal around 1708 cm^{-1}. These two bands resemble a doublet feature assigned to the $P680^+$ cation, arising from the uneven charge distribution across the two primary donor chlorophylls (Okubo et al. 2007; Nagao et al. 2017).

Three positive peaks at 1638, 1648, 1688 cm^{-1} in Fig. 2A also exhibit a decrease in intensity in Fig. 2B and C, resulting in prominent negative peaks in the double-difference spectra (Fig. 2E). The decaying negative peaks at 1680 and 1658 cm^{-1} result in positive peaks in Fig. 2E. A negative band at 1734 cm^{-1} in Fig. 2B that upshifts to 1738 cm^{-1} in Fig. 2C displays a less clear behavior, but nevertheless results in a prominent positive peak in Fig. 2E. All the aforementioned peaks have counterparts in previously reported $P680^+$/P680 spectra (Nagao et al. 2017). In fact, the entire

region between 1732 and 1520 cm^{-1} in Fig. 2E strongly resembles the shape of P680/P680$^+$ spectra (with some differences in the relative intensities of the peaks).

As outlined above, Y_Z^{ox}/Y_Z features are expected to be mostly absent in the 80 ns spectrum and to become more prominent at later time points. Y_Z^{ox} features should thus appear as positive contributions (positive peaks) in Fig. 2E, while Yz features should be negative. Comparing the signal amplitudes reported for P680$^+$/P680 and Y_Z^{ox}/Y_Z, it is evident that Y_Z^{ox}/Y_Z signals are roughly ten times less pronounced (Berthomieu et al. 1998; Nagao et al. 2017). However, the previously small amplitudes in the Y_Z^{ox}/Y_Z difference spectrum also could relate to formation of Y_Z^{ox} in a comparably small fraction of PSII only. Previously, prominent positive peaks at about 1512 and 1550 cm^{-1} alongside a negative peak at 1543 cm^{-1} have been reported (Nakamura et al. 2014; Nagao et al. 2017), which does not agree well with features in Fig. 2E. For the second and third flash difference spectra, we detect a positive peak at 1520 cm^{-1}, whereas for the first and fourth flash spectra a broad (but weak) peak around 1512 cm^{-1} may be present, possibly suggesting that the presence of an intact OEC modifies the spectral features previously reported for the Y_Z^{ox}/Y_Z difference spectrum in Mn-depleted PSII.

The features in the spectral region of Fig. 2E overall show a better agreement with features related to the P680$^+$/P680 difference spectrum. The triplet-shaped peak typically observed in Y_Z spectra around 1677–1700 cm^{-1} is also not visible in Fig. 2E. It is, however, faintly visible in Fig. 2B: when comparing Fig. 2B and C (while keeping in mind the baseline shift), the positive peaks at 1700 and 1688 cm^{-1} are clearly increasing, while a new peak at 1680 cm^{-1} forms—but the latter only in the third flash spectrum. The derivative-like group of peaks at 1550, 1542 and 1532 cm^{-1} in Fig. 2B and C also resemble previous findings in Y_Z^{ox}/Y_Z spectra; but these peaks are absent or inverted in Fig. 2D and E.

In experiments on Mn-depleted PSII particles, a differential signal of the Y_Z^{ox}/Y_Z difference spectrum has been detected at ca. 1700/1706 cm^{-1} (positive/negative peak) and assigned to perturbation of the keto C=O vibration of the P680 chlorophyll denoted as PD1 (Berthomieu et al. 1998; Nakamura et al. 2014; Nagao et al. 2017). This differential 1706/1700 cm^{-1} feature is well resolved also in the spectra of Fig. 2C (collected at 10 µs; negligible P680$^+$ population), in line with assignment to Y_Z^{ox}/Y_Z and confirming the results previously reported for Mn-depleted PSII. The double-difference spectra of Fig. 2E, however, reflect a more complex situation. In Fig. 2E, not only the Y_Z^{ox}/Y_Z features at 1700 and 1706 cm^{-1} of Fig. 2C contribute to the peaks detected at 1708 and 1698 cm^{-1}, but also prominent features of the P680$^+$/P680 difference spectrum. Comparison of the time evolution of the 1708 cm^{-1} and 1698 cm^{-1} IR signals with the P680$^+$ population (which is analyzed further below) suggests that the P680$^+$/P680 feature provides the more major contribution to the 1708/1698 cm^{-1} peaks in Fig. 2E. Also the presence of a strong negative peak at 1698 cm^{-1} in the 80 ns spectrum and the relative intensities of the 1708/1698 cm^{-1} peaks support a dominating contribution of the P680/P680$^+$ difference spectrum. We conclude that the double-difference spectrum in Fig. 2E is largely dominated by P680/P680$^+$ contributions, although Y_Z^{ox}/Y_Z features also contribute.

In light of the above conclusion, one may take a closer look at differences between Fig. 2E and the P680$^+$/P680 difference spectra in previous FTIR studies on Mn-depleted and thus O_2-inactive PSII sample. While here we see a prominent peak at 1544 cm^{-1}, this peak only appears as a small side-peak in previous reports for P680$^+$/P680. A previously reported peak at 1557 cm^{-1}, which should appear as positive in Fig. 2E, is on the other hand missing. Furthermore, the peak around 1633 cm^{-1} is much broader in our data and exhibits a clear S-state dependence, clearly indicating an influence of the OEC (and/or its environment) on these fast processes.

P680$^+$ reduction kinetics observed around 1800 cm^{-1}

Figure 3 shows the time-resolved IR difference signal following the first four excitation flashes, obtained by

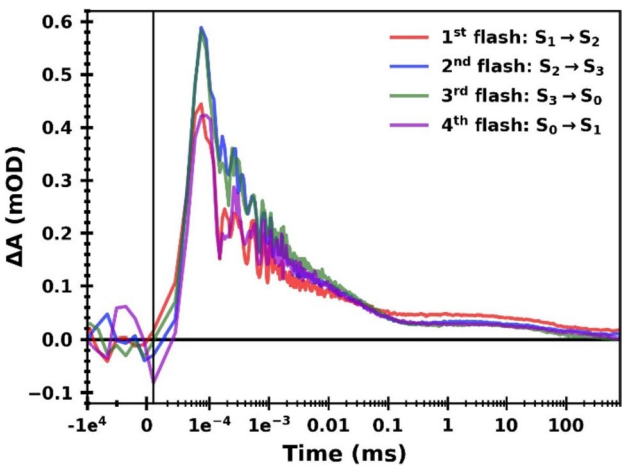

Fig. 3 Flash-induced IR difference absorption at wavenumbers greater than 1760 cm^{-1}, corresponding to the broad time-dependent background visible in the spectra in Fig. 2. All transients acquired between 1760 and 1884 cm^{-1} were averaged to improve the signal-to-noise ratio. Data associated mostly with the $S_1 \rightarrow S_2$ transition (first flash) is shown in red, the $S_2 \rightarrow S_3$ transition (second flash) in blue, the $S_3 \rightarrow S_0$ transition (third flash) in green and the $S_0 \rightarrow S_1$ (fourth flash) in magenta. The signal from 100 ns before the excitation flash up to 11.5 ns after the flash is shown on a linear scale, while the data between 11.5 ns and 800 ms is shown on a logarithmic x-axis; the two different axes are separated by a vertical line

averaging the signal at 51 individual wavenumbers in the range of 1760–1884 cm^{-1}. As seen in Fig. 2, the region above 1760 cm^{-1} exhibits a background (baseline) shift but no prominent features; the transients of the individual wavenumbers all display similar kinetics (data not shown) and were thus averaged to reduce the noise level. The four flash-induced transients in Fig. 3 show overall very similar kinetics. A rise to the maximum signal, which is higher after the second and third flash than after the first and fourth flash, occurs within about 80 ns (the delay to reaching the maximum is merely due to slow instrument response). All four transients show a multiphasic decay back to zero, whereby the first and fourth as well as the second and third flash transients show near identical behavior to each other. At around 100 µs, any S-state dependence disappears; merely the first flash transient shows a slightly up-shifted amplitude in the range from ~ 100 µs to 800 ms. The fifth flash, as well as all following flash-induced transients, do not show this upshifted signal (Fig. S4), which is thus attributed to a signal contribution of presently unknown origin exclusive associated with the first flash applied to dark-adapted PSII.

Figure 4A–C show the averaged difference absorption as a function of flash number for the data shown in Fig. 3 (and its subsequent six flashes, shown in Fig. S4) at around 80 ns, 500 ns and 10 µs, respectively. Figure 4D additionally shows the absolute values at 10 µs minus 500 ns. All four flash-number dependent IR signals show a clear quaternary oscillatory pattern with a maximum either at the second flash (Fig. 4A, B, D) or at the third flash (Fig. 4C).

This period-of-four behavior of the 1884–1760 cm^{-1} data, together with the well-established notion that a broad electronic band associated with $P680^+$ extends across the entire range from 1000 to 6000 cm^{-1} spectral region (Okubo et al. 2007), provides a strong indication that the transients in Fig. 3 are directly associated with $P680^+$ reduction kinetics of intact, oxygen-evolving PSII. The flash-number dependence (and thus S-state dependence) of the $P680^+$ background signal at 80 ns, 500 ns and 10 µs (as well as 10 µs minus 500 ns) is shown as a bar diagram in Fig. 5. All trends visible in Fig. 5 reflect a real S-state dependence because they are in line with the respective oscillatory pattern of Fig. 4. On a first glance, the S-state dependence of the maximal $P680^+$ level detected at 80 ns is surprising because each of the saturating laser flashes is expected to induce $P680^+$ formation in essentially all PSII centers, suggesting the same initial $P680^+$ level. This behavior of the here detected $P680^+$ signal is traced back to the limited time resolution of our experiment. It is explainable by a faster $P680^+$ decay time on the first and fourth flash than on the second and third flash, as illustrated by simulations of hypothetical $P680^+$ transients shown in Fig. 6.

To further characterize this $P680^+$ background signal, the transients in Fig. 3 were simulated with a sum of four

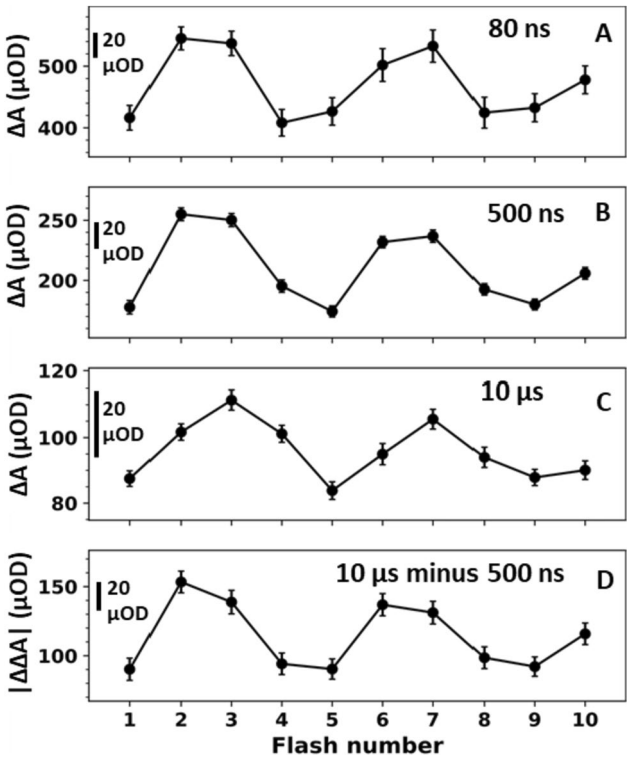

Fig. 4 Averaged IR difference absorption (ΔA) at wavenumbers greater than 1760 cm^{-1} as a function of flash number at different times after the respective excitation flash. The data shown here corresponds to the data set shown in Figs. 3 and S4. **A** IR difference absorption averaged around 80 ns (50–110 ns). **B** IR difference absorption averaged around 500 ns (250–750 ns). **C** IR difference absorption averaged around 10 µs (8–12 µs). **D** Absolute IR double difference absorption obtained by subtracting the signal around 500 ns from the signal around 10 µs (**C** minus **B**, multiplied by − 1). All averaged IR absorption values (**A**–**D**) exhibit a clear period-of-four dependency on the flash number. The error bars correspond to the standard error obtained from averaging the signal at all wavenumbers between 1760 and 1884 cm^{-1}

exponentials, taking into account the limited temporal resolution of the experiment (by convolution with the IRF as detailed in the SI). Simulated transients as obtained by least-squares fitting with calculation of the error sum for times ranging from 0 to 100 µs and the corresponding simulation parameters are shown in Figs. 7 and 8, respectively. The slowest time constant was constrained to be the same in all four transients; the other three time constants could vary freely. All amplitudes could vary freely, but the sum of all amplitudes (plus offset) was constrained to be the same in all transients, justified by the assumption that the magnitude of the initial $P680^+$ signal is the same in all S-state transitions. In line with the illustrative simulations of Fig. 6, the fit parameters of Fig. 8 show that the S-state dependence of the initial peak heights of the transients in Fig. 3 results from the fastest time constant of the second

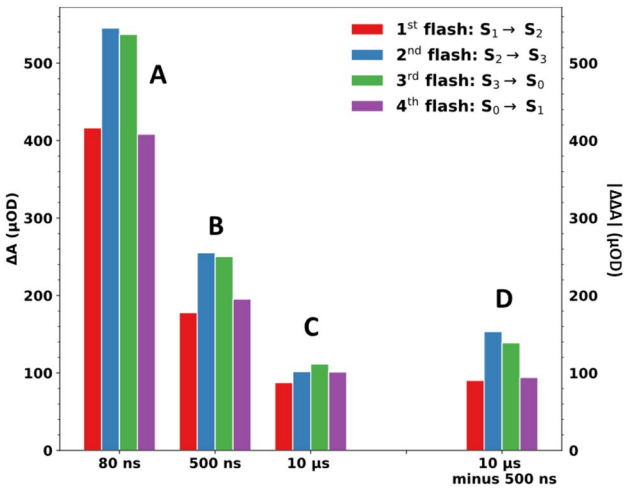

Fig. 5 Bar plot of the averaged IR difference absorption (ΔA) at > 1760 cm^{-1} at different time points following the first four excitation flashes, indicating the time- and S-state-dependent background signal of the spectral data in Fig. 2. The data shown here corresponds to the data set shown in Fig. 3 (average of all transients between 1760 and 1884 cm^{-1}). Data associated mostly with the $S_1 \rightarrow S_2$ transition (first flash) is shown in red, the $S_2 \rightarrow S_3$ transition (second flash) in blue, the $S_3 \rightarrow S_0$ transition (third flash) in green and the $S_0 \rightarrow S_1$ (fourth flash) in magenta. The IR difference absorption was averaged around **A** 80 ns (50–110 ns), **B** 500 ns (250–750 ns) and **C** 10 μs (8–12 μs). The absolute IR double difference absorption obtained by subtracting the signal around 500 ns from the signal around 10 μs (**C** minus **B**, multiplied by − 1) is shown in (**D**)

and third flash transients being slower than the fastest time constants of the first and fourth flash transients.

For all four transients, the values of the fast nanosecond time constant (τ_1, 30–50 ns)) as well as the corresponding amplitudes (highest in S_1 and S_0, lowest in S_2 and S_3) are in good agreement with previous results (Karge et al. 1996; Schilstra et al. 1998), inter alia verifying the used approach to consider the time resolution of the experiment in the least-squares curve-fit of the transients. The S-state dependence of the amplitudes of the slower nanosecond component (τ_2) is also in good agreement with previous findings on $P680^+$ kinetics (highest value after the second flash); the value for τ_2 found for the fourth flash transient (1.1 μs), however, is somewhat slower than values reported previously (Eckert and Renger 1988; Meyer et al. 1989; Lukins et al. 1996; Ahlbrink et al. 1998; Schilstra et al. 1998; Jeans et al. 2002). Both microsecond components, τ_3 (4–8 μs) and τ_4 (42 μs), are in line with previous results on $P680^+$ reduction kinetics regarding both time constant values and S-state dependence of amplitudes (Christen et al. 1998; Schilstra et al. 1998). In summary, the $P680^+$ reduction kinetics determined by analysis of absorption changes in the IR range agree very well with experimental results previously obtained by optical spectroscopy in the visible or near-infrared regime (the latter around 820 nm). Aside from non-identical temperatures during data collections, the differences in simulation parameters likely reflect variations in the used PSII preparations (in particular varying fractions of O_2-inactive PSII) or relate to details of the multi-exponential fits in the presence of significant noise contributions.

Discussion

$P680^+$/P680 and Y_Z^+/Y_Z difference spectra of intact PSII particles

Here we present the first time-resolved investigation on PSII in the mid-infrared regime that addresses the laser-flash induced [$P680^+$, Q_A^-] radical-pair state and its decay by reduction of $P680^+$ by the redox-active tyrosine (Y_Z) with multi-phasic decay kinetics. Difference spectra for the Q_A^-/Q_A, $P680^+$/P680, Y_Z^+/Y_Z transitions have been reported before based on conventional (not time-resolved) FTIR spectroscopy and sophisticated experimental protocols to 'isolate' the difference spectra assignable to reduction (Q_A^-/Q_A) or oxidation ($P680^+$/P680, Y_Z^+/Y_Z) of a specific redox-factor (Zhang et al. 1997; Berthomieu et al. 1998; Noguchi et al. 1998; Berthomieu and Hienerwadel 2005; Okubo et al. 2007; Nakamura et al. 2014; Kato et al. 2016; Nagao et al. 2017). For detecting the $P680^+$/P680 and Y_Z^+/Y_Z difference spectra, typically Mn-depleted PSII particles were employed, where the donor side of PSII had been seriously modified by removal of the Mn_4CaO_x cluster, typically in conjunction with removal of some membrane-extrinsic PSII polypeptides. The here reported time-resolved experiments now facilitate the comparison of the $P680^+$/P680 and Y_Z^+/Y_Z difference spectra between Mn-depleted and intact O_2-evolving PSII.

Overall, the double difference spectra of intact, O_2-evolving PSII (Fig. 5E) exhibit excellent agreement with the previously reported $P680^+$/P680 spectra of Mn-depleted PSII (Okubo et al. 2007) suggesting that the spectral characteristics of both P680 and $P680^+$ are not strongly affected by the presence of the Mn_4CaO_x cluster. There are clear similarities with previously reported Y_Z^+/Y_Z difference spectra of Mn-depleted PSII (Nagao et al. 2017), but also clear differences.

When compared to spectra of Mn-depleted PSII, the clear S-state dependence of many peaks provides new information. For features exclusively related to P680/$P680^+$ one might expect them to reflect the S-state dependence of the broad feature $P680^+$ detected above 1760 cm^{-1} (Fig. 5D), that is, the peak amplitudes of the second and third flash spectra are expected to be moderately enlarged compared to that of the first and fourth flash. However, some peaks (1678(+), 1664(−), 1630(+) and 1520(+) cm^{-1}) show a more pronounced S-state dependence of

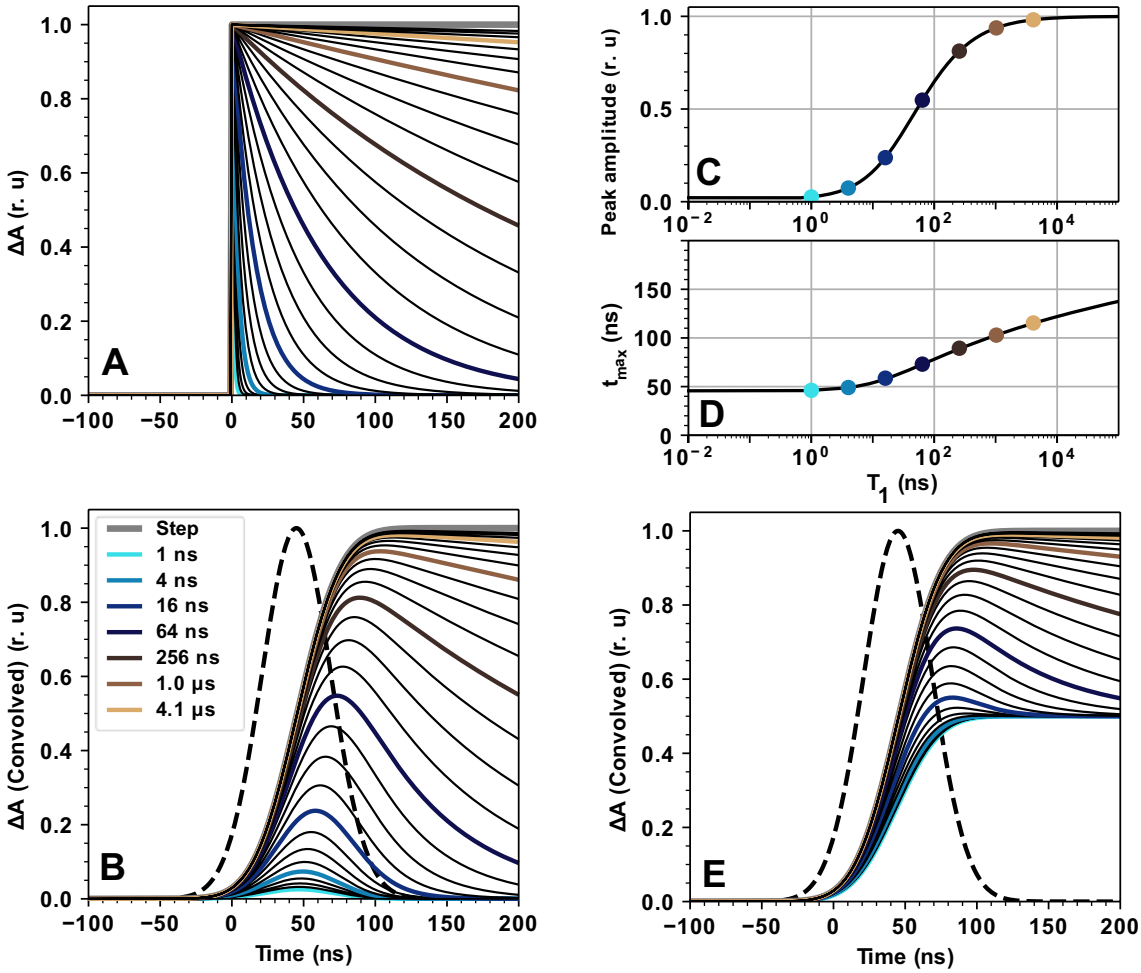

Fig. 6 Influence of a limited temporal resolution of the experimental set up, represented by a Gaussian instrument response function, on the maximal (peak) intensity and peaking time of a hypothetical $P680^+$ absorption transient. **A** Ideal absorption transients immediate $P680^+$ formation and complete $P680^+$ re-reduction by a single-exponential decay, with a hypothetical decay time varied between 1 ns and 4.1 µs (colored lines). Additionally, a hypothetical stable $P680^+$ formation (step function) is shown as a grey line. Thinner black lines indicate transients with components that lie in between the rates of neighboring color-coded transients (the decay time of neighboring curves differ by a factor of $\sqrt{2}$). **B** The transients shown in **A** convolved with a Gaussian instrument response function (IRF) with a standard width of 17 ns (dashed line) which was determined previously (Mäusle et al. 2023). **C** Influence of the $P680^+$ decay time constant on the maximal amplitude (peak amplitude) of the convolved transients of **B**. **D** Influence of the $P680^+$ decay time constant on the time of the maximal signal amplitude (t_{max}). **E** Absorption transients simulated by two exponential components convolved with the Gaussian IRF. One exponential is set to a very slow value, mimicking a step-response, while the faster exponential is varied in the same way as in **A** and **B** (1:1 amplitude ratio of fast and slow component). In **C** and **D** the colored dots represent the respective transients of **B**. In all panels the colors indicate the (fast) decay constants given in the legend shown in **B**

amplitudes than expected, while others (1708(−), 1544(+), 1366(+), 1344(+) cm^{-1}) show, within the noise-level, none. We hypothesize that the latter features could be indirectly related only to $P680^+$ and Y_Z^{ox} formation, e.g. by long-range electric field effects.

Three of the features with strongly S-state dependent amplitudes (1664(−), 1630(+) and 1520(+)) are likely related to Y_Z^{ox}/Y_Z (the following comparisons relates to the spectra reported by Nagao et al. (2017)):

(i) The negative feature at 1664 cm^{-1} in the second and third flash spectra is broader and slightly upshifted in the first and fourth flash. Y_Z^{ox}/Y_Z spectra of inactive PSII show a strong feature at 1665(−) and 1677(+), which might be the cause of this additional modulation.

(ii) The feature around 1630 cm^{-1} exhibits a small, but clear, double peak in the second and third flash spectra with an additional side peak at 1612 cm^{-1}. In con-

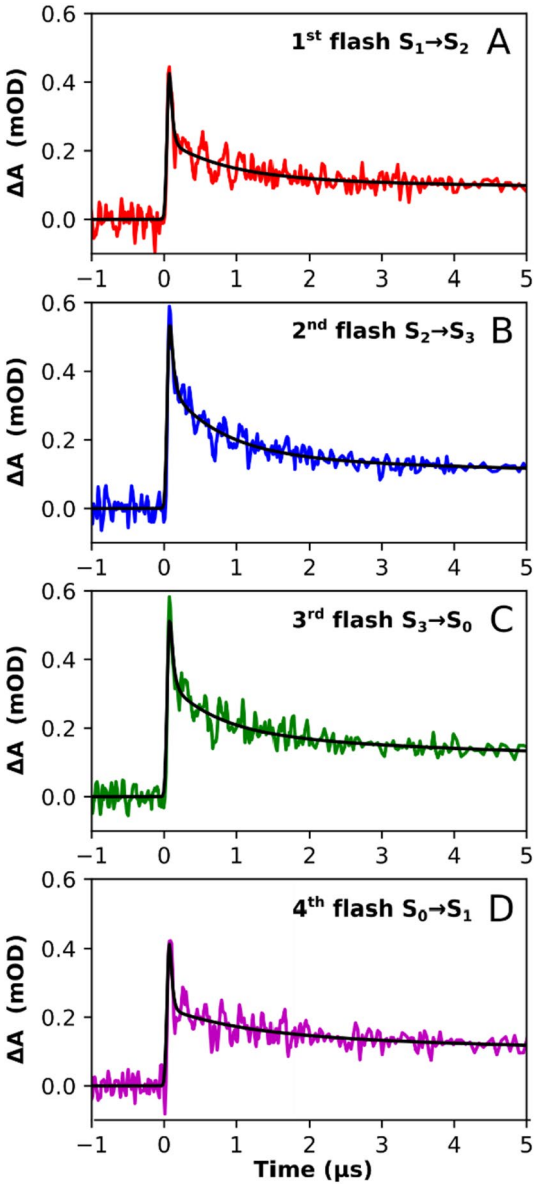

Fig. 7 Multi-exponential fits of the IR transients of wavenumbers greater than 1760 cm^{-1}, following the first four excitation flashes. The data (colored lines) corresponds to that of Fig. 3, but here shown with a linear time axis for the times ranging from 1 µs before and 5 µs after the respective laser flash. The colored lines indicate the recorded data while the black lines indicate the simulations obtained by a least-squares fit of the multi-exponential $P680^+$ decay that involves convolution with the instrument response function, to account for the limited temporal resolution of the experiment. For each of four transients shown in panel **A**–**D**, the $P680^+$ decay was simulated by a sum of four exponentials plus an offset term (y_0), taking into account the instrument response function (see "Materials and methods" section for details of the fit approach). The fit results, i.e., four amplitudes (a_1 to a_4) and four time constants (τ_1 to τ_4) for each of the transients shown in **A**–**D**, are presented in Fig. 8

trast, it appears as one broad feature in the first and fourth flash. Y_Z^{ox}/Y_Z spectra of inactive PSII show a negative peak at 1627 cm^{-1}, which could be the cause of the small dip in our data (giving the feature the appearance of a double peak). The side peak at 1612 cm^{-1} could similarly be caused by the dip around 1620 cm^{-1}, which is also present as a negative peak in Y_Z^{ox}/ Y_Z spectra of inactive PSII.

(iii) The prominent peak in the second and third flash spectra at 1520 cm^{-1} is replaced by a smaller broad feature in the first and fourth flash. From spectra of inactive PSII, we would expect a 1520(+) peak for $P680/P680^+$ and a 1512(+) peak for Y_Z^{ox}/ Y_Z. The broad feature in the first and fourth flash spectra could be a merged peak of both. Possibly the 1512 cm^{-1} Y_Z^{ox} peaks upshifts in the second and third flash, resulting in a very pronounced peak at 1520 cm^{-1}.

The relations to Y_Z^{ox}/Y_Z spectra of Mn-depleted PSII discussed above are still hypothetical, inter alia due to the possible influence of noise contributions, and require further investigation. However, irrespective of the spectral details, the pronounced S-state dependency of several spectra features implies that in future investigation the S-state specific events associated with Y_Z oxidation, which could be rearrangement of the protein-water network in the vicinity of Y_Z and the OEC as well as conformational changes of the tyrosine residue itself, may be traced by infrared spectroscopy.

Fast acceptor side processes?

The interpretation of the spectra so far was done under the assumption that acceptor-side kinetics do not contribute significantly to the IR signals in the early time domain. Indeed, the absorption at 1478 cm^{-1}, which has been assigned to a semiquinone mode (Berthomieu et al. 1990), is mostly constant between 500 ns and 10 µs after correcting for its $P680^+$ background (Fig. S8A). This implies that the quinone oxidation state does not change in this time range. Yet a closer look at other wavenumbers previously assigned to the acceptor-side (1658, 1638, 1552 and 1532 cm^{-1}; (Berthomieu et al. 1990, Noguchi et al. 1999)) reveals that they *do* exhibit changes in the above time range. Even in the absence of quinone redox-state changes these might relate to acceptor side processes, e.g., reflecting ionic or proteinaceous relaxation processes following the formation Q_A^-. For example, the negative Q_A^- charge may cause subtle rearrangement of the protein-water network at the PSII acceptor side, possibly involving proton relocations, that stabilize Q_A^- and/or are conducive regarding the subsequent Q_B reduction. It indeed has been reported that Q_A reduction induces changes at the non-heme Fe site, which however were found to be

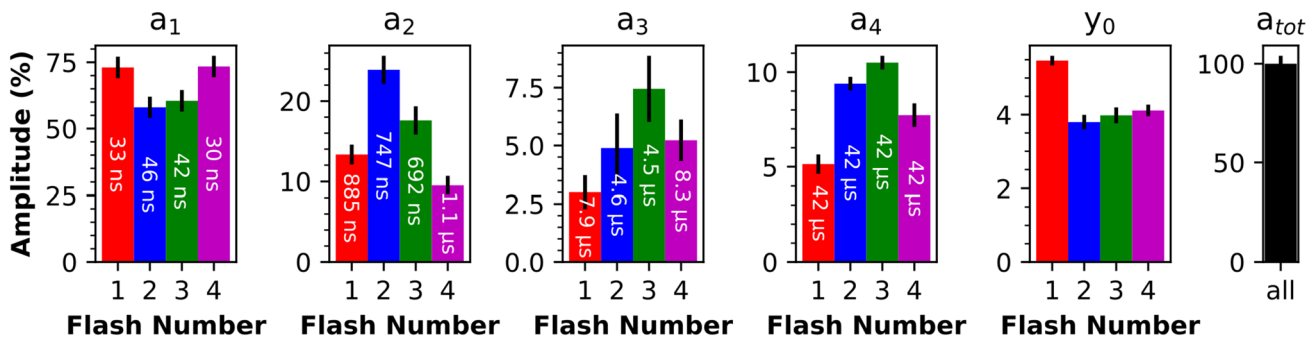

Fig. 8 Results of the multi-exponential fit of the first four flash-induced transients at greater than 1760 cm^{-1} (shown in Fig. 7). Each transient was fitted to a sum of four exponentials and an offset (y_0); the amplitudes are normalized to the sum of all amplitudes plus offset and therefore represent the relative contribution of the four components to the fitted transients. The amplitudes and time constants were free to vary, solely τ_4 was constrained to be identical in all four transients (fit range from 0 to 100 µs). The amplitudes and y_0 are shown as bar plots and the respective time constants are indicated. The 1σ uncertainty ranges of the amplitudes, obtained from the covariance matrix provided by the least squares fitting procedure, are indicated by vertical black lines. The absolute values of the amplitudes, as well as the offset, are shown in Fig. S1 and Table S2 of Supplementary Information

comparatively slow with a half-time of ca. 150 µs (Chernev et al. 2011). The possibility of acceptor side contributions to the IR signals in the time domain from 500 ns to 10 µs is discussed in the following.

At 1658 cm^{-1} the initial IR absorption changes are especially pronounced (see Fig. 2A). This could be due to either $P680^+$ or Q_A^-, which both absorb at this wavenumber. The flash-number dependency of the 1658 cm^{-1} absorption change between 500 ns and 10 µs, however, does not exhibit a period-of-two pattern (Fig. S11A). A period-of-two pattern would strongly support the contribution of an acceptor side process, whereas a period-of-four pattern is indicative of donor side processes.

Q_A^-, $P680^+$, and Y_Z^{ox} all absorb at 1638 cm^{-1} (Noguchi et al. 1999; Nagao et al. 2017), meaning we expect an initially positive IR difference signal, which decays concomitantly with decreasing Q_A^- and $P680^+$ populations, but increases as Y_Z^{ox} is formed. Between 500 ns and 10 µs we indeed observe a rise of the already positive signal before it subsequently decays (not shown); the flash-number dependency of the double-difference absorption again does not show a period-of-two, but a period-of-four behavior (Fig. S11B).

Q_A^-, $P680^+$ and Y_Z^{ox} all also have reported positive bands around 1532 cm^{-1} (Noguchi et al. 1999; Nagao et al. 2017). At this wavenumber the double-difference flash dependency might exhibit a small-amplitude period-of-two behavior on top of a larger period-of-four pattern (Fig. S11D).

In conclusion, at four wavenumbers previously assigned to quinones the flash-pattern analysis of Fig. S11 does not provide positive evidence for acceptor-side contributions to the IR signals recorded in the time range from 500 ns to 10 µs. However, this finding does not exclude acceptor side contributions induced by Q_A^- formation (which might then also mask spectral features related to $P680^+$ reduction or Y_Z oxidation). This is the case because relaxation processes that are induced by Q_A oxidation but proceed fully independently of both the Q_B site and the non-heme Fe site are not predicted to exhibit a period-of-two flash number dependency. (In our study, the non-heme Fe site undergoes flash-number dependent oxidation state changes in some PSII due to the use of PpBQ as an electron acceptor; see SI for more details.) Thus, there remains the intriguing option that IR transients may report on acceptor side processes trigged by Q_A oxidation. Future investigations along this road will be of interest.

$P680^+$ reduction kinetics observed via the broad mid-IR electronic band

By tracking time-resolved IR absorption changes at wavenumbers around 1800 cm^{-1}, which is outside the region of protein vibrations, we exploit the broad electronic $P680^+$ band (spanning roughly 1000–6000 cm^{-1}) (Okubo et al. 2007) to directly observe $P680^+$ reduction kinetics. The average of all transients between 1760 and 1884 cm^{-1} (Fig. 3) displays multi-phasic S-state dependent behavior in overall excellent agreement with other spectroscopic studies (Christen et al. 1998; Schilstra et al. 1998). Previously, the $P680^+$ decay kinetics were investigated using optical spectroscopy in the visible or near-infrared regime. Using visible-light absorption changes, the probing light also excites the PSII photochemistry; for near-IR probing light (around 820 nm), the time-dependent delayed fluorescence emission (Buchta et al. 2007; Grabolle and Dau 2007; Zaharieva et al. 2011) is sensed by the detector. While work-arounds exist, the absence of these issues when employing time-resolved IR spectroscopy can be seen as a major advantage.

This multi-phasic $P680^+$ recombination process has previously been interpreted as arising from conformational changes, possibly involving relocation of protons or water molecules, that shift the $P680^+ Y_Z \leftrightarrow P680 Y_Z^{ox}$ equilibrium more towards the right side of the equation. For example, on the second flash, the fastest phase of $P680^+$ reduction and Y_Z^{ox} formation (about 40 ns) accounts for only about 55% of the total amplitude of the $P680^+$ signal (Fig. 8). A value of 50% would correspond to equilibrium constant of unity and thus zero difference of the Gibbs free energy (ΔG_0) of the reaction. In a subsequent process with a time constant of about 750 ns, the $P680^+$ population decreases significantly, corresponding to a negative change in the free-energy difference. The simulation results of Fig. 8 suggest minimally two further processes of decreasing $P680^+$ populations, each corresponding to an increasingly negative ΔG_0.

The 40 ns phase is thought to be linked to, or preceded by, a proton-shift between His190 and Y_Z (Eckert and Renger 1988); the application of Marcus theory suggested that it is kinetically limited by a non-adiabatic ET process (Renger et al. 1998). One concept that could reconcile a rate-limiting electron transfer step with a proton transfer is that of a low barrier hydrogen bond (LBHB) between the His190 (of the D1 protein) and Y_Z (Renger 2004). Structural analysis of PSII indeed revealed that the distance of the groups in question is shorter than that of a standard H-bond (Saito et al. 2011; Kawashima et al. 2018; Ibrahim et al. 2020; Bhowmick et al. 2023).

The slow nanosecond phase and the microsecond kinetics have been assigned to local (dielectric) and large-scale (proton) relaxation processes, respectively, that further increase the probability of $P680^+$ reduction by Y_Z (Renger 2004). These steps were also interpreted to have a dual role to (i) stabilize Y_Z^{ox} and thus reduce the likelihood of charge recombination and (ii) structural changes—incl. restructuring of the protein-water network around Y_Z and the Mn_4CaO_x cluster—that prepare the OEC for the subsequent reactions (Klauss et al. 2012b). Klauss et al. also showed that the slow nanosecond events on the second flash and, to a lower extent, on the third flash are accompanied by a volume change of the protein, underlining the idea that structural changes are involved and that these differ between the S-state transitions.

The broad $P680^+$ absorption and its implications for future time-resolved IR studies

The broad electronic $P680^+$ band provides the unique opportunity to use mid-IR spectroscopy to trace $P680^+$ formation and decay in a wavenumber window (here 1760–1900 cm^{-1}) that in PSII is essentially free of distinct IR absorption lines originating from molecular vibrations. Thus, the $P680^+$ signal here obtained by detection of IR absorption changes in the range from 1760 to 1900 cm^{-1} is predicted to be free of overlapping contributions from other redox factors or further events (e.g. changing H-bond patters). Such overlap of vibration bands is typically observed in other spectral regions (at wavenumber below 1760 cm^{-1} or well above 1900 cm^{-1}), as the extended discussion of the spectra of Fig. 2 vividly illustrates. The broad, featureless $P680^+$ background signal has been exploited before for tracking the P680 redox state by detection of IR transients at 4000 cm^{-1} (Sakamoto et al. 2017). Whereas distinct IR absorption lines are not expected to contribute to the broad $P680^+$ absorption, further similarly broad absorption changes might contribute, as discussed in the following.

Protonated water clusters or strong hydrogen bonds can exhibit continuum bands that could potentially superimpose the broad $P680^+$ band (Zundel 1988). Such a strong H-bond is present between Y_Z and D1-His190; H-bonding partners and H-bond strength are changing upon Y_Z oxidation or reduction. However, the transients detected at 1884–1760 cm^{-1} do not show any temporal kinetics assignable to Y_z^{ox} reduction by the Mn_4CaO_x cluster. Thus, we can exclude any significant contribution of the Y_Z-H-His190 continuum band to the $P680^+$ signal (see Figs. 3 and S10). This does not mean that this and other continuum bands are non-existent, but their amplitude most likely is clearly smaller than that of the electronic $P680^+$ band. (The signal changes of small amplitude visible in Fig. S10 might relate to such continuum band contributions.)

Broad absorption bands associated with Q_A and Q_B have been reported between 3000 and 2500 cm^{-1} (Suzuki et al. 2005), and it is conceivable that these also extend also to the wavenumber range studied here. Indeed, the positive signal in the millisecond region of the IR transients recorded at wavenumber above 1760 cm^{-1} (Fig. 3) coincides with the presence of Q_A^- and Q_B^-; both quinones seem to contribute roughly equally (Figs. S9 and S10). We estimate their contribution to the initial $P680^+$ signal (for a detection system with high time resolution) of being around 5.5% for the first flash applied to dark-adapted PSII and around 3.5% for later flashes (Fig. S10), explaining the y_0 contribution in Fig. 8 as resulting from the quinone contribution (versus residual $P680^+$). We conclude that broad quinone-associated absorption most likely contribute to the IR background signal here assigned to $P680^+$. However, its contribution is small and likely fully negligible when discussing the $P680^+$ reduction in the time domain from nanoseconds to tens of microsecond.

What further factors influence the broad $P680^+$ absorption band and its temporal kinetics? The broad electronic band of PSII samples may be species-dependent or may be influenced by the type of PSII preparation. Okubo et al. (2007) found that PSII membranes from spinach and core complexes of *T. vestitus* exhibit a similar, but

not identically broad band; also the broad electronic $P700^+$ absorption of PSI particles shows a strong species dependency (Hastings et al. 2001). $P680^+$ kinetics differ pronouncedly between intact and Mn-depleted PSII (Haumann et al. 1997; Ahlbrink et al. 1998; Hays et al. 1999). Thus, differing ratios of intact PSII vs. O_2-inactive PSII is expected to also impact the detected $P680^+$ reduction kinetics strongly and thus the background IR signal. Experiments on often more fragile PSII core complexes with genetically modified PSII proteins may be especially strongly affected by slower $P680^+$ recombination events due an especially high fraction of O_2-inactive PSII.

The benefits of detecting $P680^+$ transients specifically in the IR regime should not obscure a possible complication relating to the broad electronic transition. Because the electronic band stretches across the entire mid-IR region, it is expected to cause a major time-dependent $P680^+$ background signal at all wavenumber in the mid-IR region. In future investigations, it may be crucial to correct for the time-dependent $P680^+$ background, because it could affect the time courses assigned to molecular vibrations significantly. An approximate correction can readily be achieved by subtraction of the $P680^+$ transients determined at wavenumbers around 1800 cm^{-1}. This approach would be accurate for a wavenumber-independent strength of the electronic $P680^+$ absorption, but approximative only for a curved $P680^+$ absorption background. However, the exact wavenumber dependence of the broad $P680^+$ absorption is not known a priori and not readily estimated. One approach for its determination could be to globally fit the time-resolved data set over the entire spectral range between 1890 and 1310 cm^{-1} with a sum of exponential functions, where as an additional summand the $P680^+$ transient determined at wavenumbers above 1760 cm^{-1} is weighted with an amplitude that varies only smoothly over the entire wavenumber range, e.g., in form of a quadratic function. We note that in the previously reported step-scan FTIR experiment on oxygen-evolving PSII (Greife et al. 2023), the mode of processing the step-scan data ensured an efficient baseline correction so that the broad electronic contributions assignable to $P680^+$ did not affect the time-resolved spectral data set significantly.

In summary, we establish an experimental approach for determination of $P680^+$ reduction kinetics in the time range from nanosecond to tens of milliseconds, which is based on detection of the broad electronic absorption band assignable to $P680^+$. This absorption band could result in misleading time-resolved data on molecular vibrations, which can be avoided by appropriate corrections; a correction mode is proposed.

Experimental progress and future developments

Here we demonstrate mid-IR experiments on the light-driven reactions of oxygen-evolving PSII that cover an extended spectral range (1310–1890 cm^{-1}) at high time resolution. The methodology is experimentally clearly more efficient than the step-scan FTIR experiment reported in Greife et al (2023).

The fast nanosecond component of 30–50 ns is at the limit of the temporal resolution of the current experimental setup. The here used approach of convolution of the ideal multi-exponential fit function with the IRF nonetheless provides reasonable results but is prone to significant imprecision in the fit parameters. Further improvement of the time resolution could lead to an increased robustness of the quantitative results (regarding values of time constants and amplitudes in multi-exponential simulations).

In summary, we believe that the present study paves the way for future time-resolved IR experiments on PSII at high spectral and temporal resolution. Further technical developments are conceivable that improve the performance of the experiment further.

Supplementary Information The online version contains supplementary material available at https://doi.org/10.1007/s11120-023-01057-3.

Acknowledgements We thank the Deutsche Forschungsgemeinschaft (DFG) for financial support from the Collaborative Research Center (SFB 1078) on Protonation Dynamics in Protein Function (Project A4/Dau).

Author contributions MYD collected all experimental data, with exception of the data in Figure 1C; SMM collected the data of Fig. 1C. MYD and JB analyzed the data and contributed to interpretation of the data; SMM and HD interpreted the data in the context of past and current research. PSS built the experimental setup; SMM and MYD improved the experimental setup; SMM wrote the data processing script. HD conceptualized and supervised the research. SMM, MYD, and HD wrote the manuscript; PSS and JB contributed to writing and revision of the manuscript; SMM coordinated preparation of the initially submitted and the revised manuscript. All authors reviewed the manuscript.

Funding Open Access funding enabled and organized by Projekt DEAL.

Data availability All data that is relevant for our conclusions is shown in the article or the Supporting Information file.

Declarations

Competing interests The authors declare no competing interests.

Open Access This article is licensed under a Creative Commons Attribution 4.0 International License, which permits use, sharing, adaptation, distribution and reproduction in any medium or format, as long as you give appropriate credit to the original author(s) and the source, provide a link to the Creative Commons licence, and indicate if changes were made. The images or other third party material in this article are included in the article's Creative Commons licence, unless indicated

otherwise in a credit line to the material. If material is not included in the article's Creative Commons licence and your intended use is not permitted by statutory regulation or exceeds the permitted use, you will need to obtain permission directly from the copyright holder. To view a copy of this licence, visit http://creativecommons.org/licenses/by/4.0/.

References

Ahlbrink R, Haumann M, Cherepanov D, Boegershausen O, Mulkidjanian A, Junge W (1998) Function of tyrosine-Z in water oxidation by photosystem II: electrostatical promotor instead of hydrogen abstractor. Biochemistry 37:1131–1142. https://doi.org/10.1021/bi9719152

Babcock GT, Sauer K (1975) A rapid, light-induced transient in electron paramagnetic resonance signal II activated upon inhibition of photosynthetic oxygen evolution. Biochim Biophys Acta 376:315–328. https://doi.org/10.1016/0005-2728(75)90024-9

Berthold DA, Babcock GT, Yocum CF (1981) A highly resolved, oxygen-evolving photosystem-II preparation from spinach thylakoid membranes—EPR and electron-transport properties. FEBS Lett 134:231–234. https://doi.org/10.1016/0014-5793(81)80608-4

Berthomieu C, Hienerwadel R (2005) Vibrational spectroscopy to study the properties of redox-active tyrosines in photosystem II and other proteins. Biochim Biophys Acta 1707:51–66. https://doi.org/10.1016/j.bbabio.2004.03.011

Berthomieu C, Nabedryk E, Mantele W, Breton J (1990) Characterization by FTIR spectroscopy of the photoreduction of the primary quinone acceptor Q_A in photosystem II. FEBS Lett 269:363–367. https://doi.org/10.1016/0014-5793(90)81194-S

Berthomieu C, Hienerwadel R, Boussac A, Breton J, Diner BA (1998) Hydrogen bonding of redox-active tyrosine Z of photosystem II probed by FTIR difference spectroscopy. Biochemistry 37:10547–10554. https://doi.org/10.1021/bi980788m

Bhowmick A, Hussein R, Bogacz I, Simon PS, Ibrahim M, Chatterjee R, Doyle MD, Cheah MH, Fransson T, Chernev P, Kim I-S, Makita H, Dasgupta M, Kaminsky CJ, Zhang M, Gätcke J, Haupt S, Nangca II, Keable SM, Aydin AO, Tono K, Owada S, Gee LB, Fuller FD, Batyuk A, Alonso-Mori R, Holton JM, Paley DW, Moriarty NW, Mamedov F, Adams PD, Brewster AS, Dobbek H, Sauter NK, Bergmann U, Zouni A, Messinger J, Kern J, Yano J, Yachandra VK (2023) Structural evidence for intermediates during O_2 formation in photosystem II. Nature 617:629–636. https://doi.org/10.1038/s41586-023-06038-z

Breton J, Nabedryk E, Parson WW (1992) A new infrared electronic transition of the oxidized primary electron donor in bacterial reaction centers: a way to assess resonance interactions between the bacteriochlorophylls. Biochemistry 31:7503–7510. https://doi.org/10.1021/bi00148a010

Breton J, Nabedryk E, Leibl W (1999) FTIR study of the primary electron donor of photosystem I (P700) revealing delocalization of the charge in $P700^+$ and localization of the triplet character in ^{3}P700. Biochemistry 38:11585–11592. https://doi.org/10.1021/bi991216k

Brettel K, Schlodder E, Witt HT (1984) Nanosecond reduction kinetics of photooxidized chlorophyll-a_{II} (P-680) in single flashes as a probe for the electron pathway, H^+-release and charge accumulation in the O_2-evolving complex. Biochim Biophys Acta 766:403–415. https://doi.org/10.1016/0005-2728(84)90256-1

Buchta J, Grabolle M, Dau H (2007) Photosynthetic dioxygen formation studied by time-resolved delayed fluorescence measurements—method, rationale, and results on the activation energy of dioxygen formation. Biochim Biophys Acta 1767:565–574. https://doi.org/10.1016/j.bbabio.2007.04.003

Chernev P, Zaharieva I, Dau H, Haumann M (2011) Carboxylate shifts steer inter-quinone electron transfer in photosynthesis. J Biol Chem 286:5368–5374. https://doi.org/10.1074/jbc.M110.202879

Christen G, Renger G (1999) The role of hydrogen bonds for the multiphasic $P680^{+\bullet}$ reduction by Y_Z in photosystem II with intact oxygen evolution capacity. Analysis of kinetic H/D isotope exchange effects. Biochemistry 38:2068–2077. https://doi.org/10.1021/bi982188t

Christen G, Reifarth F, Renger G (1998) On the origin of the '35-µs kinetics' of $P680^{+\bullet}$ reduction in photosystem II with an intact water oxidising complex. FEBS Lett 429:49–52. https://doi.org/10.1016/S0014-5793(98)00552-3

Christen G, Seeliger A, Renger G (1999) $P680^{+\bullet}$ reduction kinetics and redox transition probability of the water oxidizing complex as a function of pH and H/D isotope exchange in spinach thylakoids. Biochemistry 38:6082–6092. https://doi.org/10.1021/bi9827520

Cox N, Pantazis DA, Neese F, Lubitz W (2015) Artificial photosynthesis: understanding water splitting in nature. Interface Focus 5:20150009. https://doi.org/10.1098/rsfs.2015.0009

Cox N, Pantazis DA, Lubitz W (2020) Current understanding of the mechanism of water oxidation in photosystem II and its relation to XFEL data. Annu Rev Biochem 89:795–820. https://doi.org/10.1146/annurev-biochem-011520-104801

Dau H, Haumann M (2007) Eight steps preceding O–O bond formation in oxygenic photosynthesis—a basic reaction cycle of the photosystem II manganese complex. Biochim Biophys Acta 1767:472–483. https://doi.org/10.1016/j.bbabio.2007.02.022

Dau H, Zaharieva I (2009) Principles, efficiency, and blueprint character of solar-energy conversion in photosynthetic water oxidation. Acc Chem Res 42:1861–1870. https://doi.org/10.1021/ar900225y

Dau H, Limberg C, Reier T, Risch M, Roggan S, Strasser P (2010) The mechanism of water oxidation: from electrolysis via homogeneous to biological catalysis. ChemCatChem 2:724–761. https://doi.org/10.1002/cctc.201000126

Debus RJ (2015) FTIR studies of metal ligands, networks of hydrogen bonds, and water molecules near the active site Mn_4CaO_5 cluster in photosystem II. Biochim Biophys Acta 1847:19–34. https://doi.org/10.1016/j.bbabio.2014.07.007

Eckert HJ, Renger G (1988) Temperature dependence of $P680^+$ reduction in O_2-evolving PS II membrane fragments at different redox states S_i of the water oxidizing system. FEBS Lett 236:425–431. https://doi.org/10.1016/0014-5793(88)80070-X

Eckert HJ, Wiese N, Bernarding J, Eichler HJ, Renger G (1988) Analysis of the electron transfer from $Pheo^-$ to Q_A in PS II membrane fragments from spinach by time resolved 325 nm absorption changes in the picosecond domain. FEBS Lett 240:153–158. https://doi.org/10.1016/0014-5793(88)80358-2

Gläser M, Wolff C, Renger G (1976) Indirect evidence for a very fast recovery kinetics of chlorophyll-a_{II} in spinach chloroplasts. Zeitschrift Für Naturforschung C 31:712–721. https://doi.org/10.1515/znc-1976-11-1216

Grabolle M, Dau H (2007) Efficiency and role of loss processes in light-driven water oxidation by PSII. Physiol Plantarum 131:50–63. https://doi.org/10.1111/j.1399-3054.2007.00941.x

Greife P, Schönborn M, Capone M, Assunção R, Narzi D, Guidoni L, Dau H (2023) The electron–proton bottleneck of photosynthetic oxygen evolution. Nature 617:623–628. https://doi.org/10.1038/s41586-023-06008-5

Hastings G, Ramesh V, Wang R, Sivakumar V, Webber A (2001) Primary donor photo-oxidation in photosystem I: a re-evaluation of ($P700^+$ − P700) Fourier transform infrared difference spectra. Biochemistry 40:12943–12949. https://doi.org/10.1021/bi0155753

Haumann M, Bögershausen O, Cherepanov D, Ahlbrink R, Junge W (1997) Photosynthetic oxygen evolution: H/D isotope effects and

the coupling between electron and proton transfer during the redox reactions at the oxidizing side of photosystem II. Photosynth Res 51:193–208. https://doi.org/10.1023/A:1005861917596

Hays AM, Vassiliev IR, Golbeck JH, Debus RJ (1999) Role of D1-His190 in the proton-coupled oxidation of tyrosine Y_Z in manganese-depleted photosystem II. Biochemistry 38:11851–11865. https://doi.org/10.1021/bi990716a

Hienerwadel R, Boussac A, Breton J, Berthomieu C (1996) Fourier transform infrared difference study of tyrosine$_D$ oxidation and plastoquinone Q_A reduction in photosystem II. Biochemistry 35:15447–15460. https://doi.org/10.1021/bi961952d

Ibrahim M, Fransson T, Chatterjee R, Cheah MH, Hussein R, Lassalle L, Sutherlin KD, Young ID, Fuller FD, Gul S, Kimc I-S, Simon PS, Lichtenberg Cd, Chernev P, Bogacz I, Pham CC, Orville AM, Saichek N, Northen T, Batyuk A, Carbajo S, Alonso-Mori R, Tono K, Owada S, Bhowmick A, Bolotovsky R, Mendez D, Moriarty NW, Holton JM, Dobbek H, Brewster AS, Adams PD, Sauter NK, Bergmann U, Zouni A, Messinger J, Kern J, Yano VKYaJ (2020) Untangling the sequence of events during the $S_2 \rightarrow S_3$ transition in photosystem II and implications for the water oxidation mechanism. Proc Natl Acad Sci USA 117:12624–12635. https://doi.org/10.1073/pnas.200052911

Jeans C, Schilstra MJ, Klug DR (2002) The temperature dependence of $P680^+$ reduction in oxygen-evolving photosystem II. Biochemistry 41:5015–5023. https://doi.org/10.1021/bi0118862

Junge W (2019) Oxygenic photosynthesis: history, status and perspective. Q Rev Biol 52:E1. https://doi.org/10.1017/S0033583518000112

Karge M, Irrgang KD, Sellin S, Feinaugle R, Liu B, Eckert HJ, Eichler HJ, Renger G (1996) Effects of hydrogen/deuterium exchange on photosynthetic water cleavage in PS II core complexes from spinach. FEBS Lett 378:140–144. https://doi.org/10.1016/0014-5793(95)01433-0

Kato Y, Ishii R, Noguchi T (2016) Comparative analysis of the interaction of the primary quinone Q_A in intact and Mn-depleted photosystem II membranes using light-induced ATR-FTIR spectroscopy. Biochemistry 55:6355–6358. https://doi.org/10.1021/acs.biochem.6b01052

Kawashima K, Saito K, Ishikita H (2018) Mechanism of radical formation in the H-bond network of D1-Asn298 in photosystem II. Biochemistry 57:4997–5004. https://doi.org/10.1021/acs.biochem.8b00574

Klauss A, Haumann M, Dau H (2012a) Alternating electron and proton transfer steps in photosynthetic water oxidation. Proc Natl Acad Sci USA 109:16035–16040. https://doi.org/10.1073/pnas.1206266109

Klauss A, Sikora T, Suss B, Dau H (2012b) Fast structural changes (200–900ns) may prepare the photosynthetic manganese complex for oxidation by the adjacent tyrosine radical. Biochim Biophys Acta 1817:1196–1207. https://doi.org/10.1016/j.bbabio.2012.04.017

Kok B, Forbush B, McGloin M (1970) Cooperation of charges in photosynthetic O_2 evolution-I. A linear four-step mechanism. Photochem Photobiol 11:457–475. https://doi.org/10.1111/j.1751-1097.1970.tb06017.x

Kühn P, Eckert H-J, Eichler H, Renger G (2004) Analysis of the $P680^{+\cdot}$ reduction pattern and its temperature dependence in oxygen-evolving PS II core complexes from thermophilic cyanobacteria and higher plants. Phys Chem Chem Phys 6:4838–4843. https://doi.org/10.1039/B407656G

Lubitz W, Chrysina M, Cox N (2019) Water oxidation in photosystem II. Photosynth Res 142:105–125. https://doi.org/10.1007/s11120-019-00648-3

Lukins PB, Post A, Walker PJ, Larkum AW (1996) $P680^+$ reduction in oxygen-evolving photosystem II core complexes. Photosynth Res 49:209–221. https://doi.org/10.1007/BF00034782

Mäusle SM, Abzaliyeva A, Greife P, Simon PS, Perez R, Zilliges Y, Dau H (2020) Activation energies for two steps in the $S_2 \rightarrow S_3$ transition of photosynthetic water oxidation from time-resolved single-frequency infrared spectroscopy. J Chem Phys 153:215101. https://doi.org/10.1063/5.0027995

Mäusle SM, Agarwala N, Eichmann VG, Dau H, Nürnberg DJ, Hastings G (2023) Nanosecond time-resolved infrared spectroscopy for the study of electron transfer in photosystem I. Photosynth Res. https://doi.org/10.1007/s11120-023-01035-9

Meyer B, Schlodder E, Dekker JP, Witt HT (1989) O_2 evolution and Chl a^{+II} ($P\text{-}680^+$) nanosecond reduction kinetics in single flashes as a function of pH. Biochim Biophys Acta 974:36–43. https://doi.org/10.1016/S0005-2728(89)80163-X

Nagao R, Yamaguchi M, Nakamura S, Ueoka-Nakanishi H, Noguchi T (2017) Genetically introduced hydrogen bond interactions reveal an asymmetric charge distribution on the radical cation of the special-pair chlorophyll P680. J Biol Chem 292:7474–7486. https://doi.org/10.1074/jbc.M117.781062

Nakamura S, Nagao R, Takahashi R, Noguchi T (2014) Fourier transform infrared detection of a polarizable proton trapped between photooxidized tyrosine Y_Z and a coupled histidine in photosystem II: relevance to the proton transfer mechanism of water oxidation. Biochemistry 53:3131–3144. https://doi.org/10.1021/bi500237y

Noguchi T (2010) Fourier transform infrared spectroscopy of special pair bacteriochlorophylls in homodimeric reaction centers of heliobacteria and green sulfur bacteria. Photosynth Res 104:321–331. https://doi.org/10.1007/s11120-009-9509-0

Noguchi T (2015) Fourier transform infrared difference and time-resolved infrared detection of the electron and proton transfer dynamics in photosynthetic water oxidation. Biochim Biophys Acta 1847:35–45. https://doi.org/10.1016/j.bbabio.2014.06.009

Noguchi T, Tomo T, Inoue Y (1998) Fourier transform infrared study of the cation radical of P680 in the photosystem II reaction center: evidence for charge delocalization on the chlorophyll dimer. Biochemistry 37:13614–13625. https://doi.org/10.1021/bi9812975

Noguchi T, Inoue Y, Tang X-S (1999) Hydrogen bonding interaction between the primary quinone acceptor Q_A and a histidine side chain in photosystem II as revealed by Fourier transform infrared spectroscopy. Biochemistry 38:399–403. https://doi.org/10.1021/bi982294v

Noguchi T, Suzuki H, Tsuno M, Sugiura M, Kato C (2012) Time-resolved infrared detection of the proton and protein dynamics during photosynthetic oxygen evolution. Biochemistry 51:3205–3214. https://doi.org/10.1021/bi300294n

Nuijs AM, Vangorkom HJ, Plijter JJ, Duysens LNM (1986) Primary-charge separation and excitation of chlorophyll *a* in photosystem II particles from spinach as studied by picosecond absorbance-difference spectroscopy. Biochim Biophys Acta 848:167–175. https://doi.org/10.1016/0005-2728(86)90038-1

Okubo T, Tomo T, Sugiura M, Noguchi T (2007) Perturbation of the structure of P680 and the charge distribution on its radical cation in isolated reaction center complexes of photosystem II as revealed by Fourier transform infrared spectroscopy. Biochemistry 46:4390–4397. https://doi.org/10.1021/bi700157n

Renger G (2004) Coupling of electron and proton transfer in oxidative water cleavage in photosynthesis. Biochim Biophys Acta 1655:195–204. https://doi.org/10.1016/j.bbabio.2003.07.007

Renger G, Christen G, Karge M, Eckert H-J, Irrgang K-D (1998) Application of the Marcus theory for analysis of the temperature dependence of the reactions leading to photosynthetic water oxidation: results and implications. J Biol Inorg Chem 3:360–366. https://doi.org/10.1007/s007750050245

Saito K, Shen J-R, Ishida T, Ishikita H (2011) Short hydrogen bond between redox-active tyrosine Y_Z and D1-His190 in the photosystem II crystal structure. Biochemistry 50:9836–9844. https://doi.org/10.1021/bi201366j

Sakamoto H, Shimizu T, Nagao R, Noguchi T (2017) Monitoring the reaction process during the $S_2 \rightarrow S_3$ transition in photosynthetic water oxidation using time-resolved infrared spectroscopy. J Am Chem Soc 139:2022–2029. https://doi.org/10.1021/jacs.6b11989

Schiller H, Dau H (2000) Preparation protocols for high-activity photosystem II membrane particles of green algae and higher plants, pH dependence of oxygen evolution and comparison of the S_2-state multiline signal by X-band EPR spectroscopy. J Photochem Photobiol B 55:138–144. https://doi.org/10.1016/S1011-1344(00)00036-1

Schilstra MJ, Rappaport F, Nugent JHA, Barnett CJ, Klug DR (1998) Proton/hydrogen transfer affects the S-state-dependent microsecond phases of $P680^+$ reduction during water splitting. Biochemistry 37:3974–3981. https://doi.org/10.1021/bi9713815

Schlodder E, Brettel K, Witt HT (1985) Relation between microsecond reduction kinetics of photooxidized chlorophyll a_{II} (P-680) and photosynthetic water oxidation. Biochim Biophys Acta 808:123–131. https://doi.org/10.1016/0005-2728(85)90034-9

Shevela D, Kern JF, Govindjee G, Messinger J (2023) Solar energy conversion by photosystem II: principles and structures. Photosynth Res 156:79–307. https://doi.org/10.1007/s11120-022-00991-y

Styring S, Sjöholm J, Mamedov F (2012) Two tyrosines that changed the world: Interfacing the oxidizing power of photochemistry to water splitting in photosystem II. Biochim Biophys Acta 1817:76–87. https://doi.org/10.1016/j.bbabio.2011.03.016

Suzuki H, Nagasaka M-a, Sugiura M, Noguchi T (2005) Fourier transform infrared spectrum of the secondary quinone electron acceptor Q_B in photosystem II. Biochemistry 44:11323–11328. https://doi.org/10.1021/bi051237g

Takahashi R, Hasegawa K, Noguchi T (2008) Effect of charge distribution over a chlorophyll dimer on the redox potential of P680 in photosystem II as studied by density functional theory calculations. Biochemistry 47:6289–6291. https://doi.org/10.1021/bi8007998

Takemoto H, Sugiura M, Noguchi T (2019) Proton release process during the S_2-to-S_3 transition of photosynthetic water oxidation as revealed by the pH dependence of kinetics monitored by time-resolved infrared spectroscopy. Biochemistry 58:4276–4283. https://doi.org/10.1021/acs.biochem.9b00680

Umena Y, Kawakami K, Shen J-R, Kamiya N (2011) Crystal structure of oxygen-evolving photosystem II at a resolution of 1.9 Å. Nature 473:55–60. https://doi.org/10.1038/nature09913

Vinyard DJ, Brudvig GW (2017) Progress toward a molecular mechanism of water oxidation in photosystem II. Annu Rev Phys Chem 68(68):101–116. https://doi.org/10.1146/annurev-physchem-052516-044820

Zaharieva I, Wichmann JM, Dau H (2011) Thermodynamic limitations of photosynthetic water oxidation at high proton concentrations. J Biol Chem 286:18222–18228. https://doi.org/10.1074/jbc.M111.237941

Zhang HM, Razeghifard MR, Fischer G, Wydrzynski T (1997) A time-resolved FTIR difference study of the plastoquinone Q_A and redox-active tyrosine Y_Z interactions in photosystem II. Biochemistry 36:11762–11768. https://doi.org/10.1021/bi970815t

Zundel G (1988) Proton transfer in and proton polarizability of hydrogen bonds: IR and theoretical studies regarding mechanisms in biological systems. J Mol Struct 177:43–68. https://doi.org/10.1016/0022-2860(88)80078-4

Publisher's Note Springer Nature remains neutral with regard to jurisdictional claims in published maps and institutional affiliations.